



## Modelling optically pumped magnetometer interference in MEG as a spatially homogeneous magnetic field

Tim M. Tierney<sup>a,\*</sup>, Nicholas Alexander<sup>a</sup>, Stephanie Mellor<sup>a</sup>, Niall Holmes<sup>b</sup>, Robert Seymour<sup>a</sup>, George C. O'Neill<sup>a</sup>, Eleanor A. Maguire<sup>a</sup>, Gareth R. Barnes<sup>a</sup>

<sup>a</sup> Wellcome Centre for Human Neuroimaging, UCL Queen Square Institute of Neurology, University College London, 12 Queen Square, London WC1N 3AR, UK

<sup>b</sup> Sir Peter Mansfield Imaging Centre, School of Physics and Astronomy, University of Nottingham, Nottingham, NG7 2RD, UK

### A B S T R A C T

Here we propose that much of the magnetic interference observed when using optically pumped magnetometers for MEG experiments can be modeled as a spatially homogeneous magnetic field. We show that this approximation reduces sensor level variance and substantially improves statistical power. This model does not require knowledge of the underlying neuroanatomy nor the sensor positions. It only needs information about the sensor orientation. Due to the model's low rank there is little risk of removing substantial neural signal. However, we provide a framework to assess this risk for any sensor number, design or subject neuroanatomy. We find that the risk of unintentionally removing neural signal is reduced when multi-axis recordings are performed. We validated the method using a binaural auditory evoked response paradigm and demonstrated that removing the homogeneous magnetic field increases sensor level SNR by a factor of 3. Considering the model's simplicity and efficacy, we suggest that this homogeneous field correction can be a powerful preprocessing step for arrays of optically pumped magnetometers.

### 1. Introduction

As Optically Pumped Magnetometers (OPMs) are capable of measuring magnetic fields as small as a few femtotesla (Kominis et al., 2003) they have been increasingly used to measure the magnetic fields produced by electrical current flow in the brain (Boto et al., 2018; Iivanainen et al., 2019b; Limes et al., 2020; Vivekananda et al., 2020). In this context the separation of brain signal from external magnetic interference can be challenging. External magnetic interference can arise from a number of sources such as nearby trains (Holmes et al., 2019), power-line noise (de Cheveigné, 2020), mechanical room vibration (Okada et al., 2016), or from the Earth's magnetic field (Limes et al., 2020). All of these signals may be much larger than the magnetic fields associated with brain activity and have therefore inspired a number of distinct approaches to minimize their impact.

Hardware developments to mitigate interference include active shielding systems to null low-frequency fields around the participant's head (Holmes et al., 2019; Iivanainen et al., 2019a). This approach is attractive as it allows simplification of the helmet design (to comprise just the magnetometers). Furthermore, these coils have made feasible the imaging of neural responses during participant movement (Boto et al., 2019; Holmes et al., 2018, 2019). Whilst these coils prevent artefacts in the region of 0–1Hz (with in excess of 40 dB shielding) that would move the sensors outside their dynamic range, they do not correct for the subtler modulations at higher frequencies. This interference could theoretically be corrected with high dynamic range field nulling coils capable of producing both the large static fields and time-varying fields of

much smaller magnitude. Likewise, interference due to head-movement could be reduced by incorporating higher order magnetic field gradients but all of these modifications further complicate the hardware development.

Another hardware option is to configure the sensors as gradiometers, which have excellent noise suppression (Colombo et al., 2016; Nardelli et al., 2020; Sheng et al., 2017) and are capable of unshielded neural recordings (Limes et al., 2020), providing shielding factors of 40–60 dB. Axial gradiometers typically have a baseline that is 1–2 times larger than the distance to the brain region of interest (Hämäläinen et al., 1993). Consequently, optimum baselines as large as 5 cm have been suggested (Fife et al., 1999). However, even though sensors with much smaller baselines (2 cm) do exist (Nardelli et al., 2020) the choice between baseline length and interference suppression is one of compromise. Shorter baselines reduce sensitivity to deeper sources but have improved noise suppression. This constraint may place a limit on the wearability of atomic gradiometer systems if deeper brain structures are of interest (Barry et al., 2019; Tierney et al., 2020a). In contrast, optically pumped magnetometers (Osborne et al., 2018) typically require considerable active and passive shielding (~60–80 dB at DC for our current magnetically shielded room) for successful MEG recordings (Barry et al., 2019; Lin et al., 2019; Tierney et al., 2018, 2020a). The appeal of magnetometers lies in their simplicity of construction, compact size and extreme sensitivity (Allred et al., 2002; Kominis et al., 2003).

In addition to hardware developments, there are a number of software approaches that can be used to reduce interference. Some of the most widely used methods are the Signal Space Separation (SSS) method

\* Corresponding author.

E-mail address: [tim.tierney.12@ucl.ac.uk](mailto:tim.tierney.12@ucl.ac.uk) (T.M. Tierney).

<https://doi.org/10.1016/j.neuroimage.2021.118484>.

Received 30 November 2020; Received in revised form 19 July 2021; Accepted 18 August 2021

Available online 19 August 2021.

1053-8119/© 2021 Published by Elsevier Inc. This is an open access article under the CC BY-NC-ND license (<http://creativecommons.org/licenses/by-nc-nd/4.0/>)

(Taulu and Kajola, 2005), which can achieve shielding factors greater than 40 dB (Taulu et al., 2005), the Signal Space Projection (SSP) method (Uusitalo and Ilmoniemi, 1997), with demonstrated shielding of 20–40 dB (Okada et al., 2016) and the Dual Signal Subspace Projection (DSSP) method (Sekihara et al., 2016). All methods aim to partition the data into separate subspaces that originate from inside the brain and outside the brain. Once these subspaces are defined the temporal intersection of these subspaces can be used to further reduce interference (Golub and Van Loan, 1996). When this temporal extension is used with SSS it is referred to as tSSS (Taulu and Hari, 2009). The methods diverge in the form of the basis sets used to represent the neural and external subspace. SSS uses two sets of spherical harmonics of different shape to describe magnetic fields that originate from either the inside or outside of the head. DSSP uses the eigenmodes of the lead fields to define the neural space while the nullspace of the neural space defines the external space. In SSP, the leading eigenvectors of a covariance matrix obtained from an empty room noise recording form the basis for the noise subspace. These methods make a number of assumptions that should be considered before use with small channel (< 50 in this study) OPM systems. For instance, inherent to DSSP is the assumption that the rank of the data is much greater than the rank of the lead fields. This is clearly the case in cryogenic MEG systems that may have 300 sensors and a lead field rank in the range of 50–100 (Iivanainen et al., 2020; Nenonen et al., 2007; Tierney et al., 2020b). In OPM systems this may not be the case and the rank of the lead fields may be comparable to the rank of the data because typical systems currently operate with fewer than 50 sensors (Hill et al., 2020). Similarly, in SSS the rank of the external subspace (typically 16) may share significant variance with the leadfields of small channel systems (< 50 sensors). Typical application of SSS requires that there are more channels than spherical harmonics used to model the data (default values would require greater than 95 sensors). To mitigate this issue, one could use lower order spherical harmonics as the basis set defining the external subspace. If one were to use the first order harmonics of the external subspace the basis set would consist of three terms representing the homogeneous (or constant) magnetic field in the three principal axes.

While we do not expect any interfering magnetic field to be exactly constant in space, we may approximate this interfering field as a spatially constant field. Such an approximation may not be physically correct, but we will show it to be useful for interference mitigation for two reasons. Firstly, the model is very low order (rank 3-the orthogonal spatial axes) and should therefore share minimal variance with the lead fields. Second, because of its simplicity, it can be updated in real time and track interference that is modulated by participant movement. We will motivate its use in the next section with a toy problem of parallel sensors.

## 2. Theory

### 2.1. Magnetic interference is approximately spatially constant

This effect is the basis of all gradiometer based MEG systems and has been extensively described elsewhere (Hämäläinen et al., 1993; Vrba and Robinson, 2002). We restate it here for completeness. The interfering signal measured by a sensor ( $S_1$ ) on the head is inversely proportional to the square of the distance ( $r$ ) to the interfering field's source.

$$S_1 \propto 1/r^2 \quad (1)$$

The signal experienced ( $S_{rel}$ ) by a parallel sensor, relative to  $S_1$ , displaced a distance  $r + h$  from the interference source can be described as

$$S_{rel} = r^2 / (r + h)^2 \quad (2)$$

By way of example, consider two sensors either side of a participant's head. In this case  $h \approx 20$  cm. When the distance to the interference is

much greater than the head size ( $r \gg h$ ), the relative signal is approximately constant as a function of space

$$S_{rel} \approx \frac{r^2}{r^2} = 1 \quad (3)$$

As such, we argue that much of the interference encountered in OPM systems arising from distant sources can be described by a spatially constant term (a homogeneous field). It should be noted that this term will automatically be removed in gradiometer systems and will be of most benefit to systems based on magnetometers. To estimate these spatially homogeneous field components we propose a simple model. The measured magnetic field at a point ( $b_{measured}$ ) can be described as a linear combination of the vector components ( $b_x, b_y, b_z$ ) of the magnetic field. The linear combination is determined by the unit normal of the sensor's sensitive axis ( $o_x, o_y, o_z$ ).

$$b_{measured} = o_x b_x + o_y b_y + o_z b_z \quad (4)$$

As the homogeneous vector components do not change over space we can represent the measured field at  $n$  multiple independent positions in a compact matrix form

$$\begin{pmatrix} b_{measured}^1 \\ \vdots \\ b_{measured}^n \end{pmatrix} = \begin{pmatrix} o_x^1 & o_y^1 & o_z^1 \\ \vdots & \vdots & \vdots \\ o_x^n & o_y^n & o_z^n \end{pmatrix} \begin{pmatrix} b_x \\ b_y \\ b_z \end{pmatrix} \quad (5)$$

Which can be equivalently expressed as

$$B_{measured} = N B_{homogeneous} \quad (6)$$

Where  $B_{measured}$  is the matrix representation of the measured magnetic field. The unit normal matrix ( $N$ ) is simply the row-wise concatenation of the  $n$  unit normal and  $B_{homogeneous}$  is the matrix representation of the homogeneous magnetic field components. The homogeneous components can then be estimated by premultiplying the measured magnetic field ( $B_{measured}$ ) with the pseudoinverse of the unit normal matrix ( $N^+$ )

$$B_{homogeneous} = N^+ B_{measured} \quad (7)$$

This homogeneous term ( $B_{homogeneous}$ ) should explain the majority of interference from distant sources when the participant is stationary. We note that when a participant moves, one could incorporate linear gradient terms. These would be quite beneficial for very low frequency studies (<3 Hz), designing a model informed closed loop OPM systems (Nardelli et al., 2020) or for informing coil currents in active shielding systems (Holmes et al., 2019). However, for simplicity we will ignore these higher order terms here and just focus on the benefits of using a very simple homogeneous field approximation. For an equivalent derivation of how to estimate this homogeneous field component using SSS see Appendix I.

### 2.2. The separation of signal and interference

Once the basis set ( $N$ ) is defined the  $n \times n$  homogeneous field projection matrix ( $M$ ) can be constructed as follows

$$M = I - N N^+ \quad (8)$$

Where  $I$  signifies the identity matrix and  $N^+$  is the pseudoinverse of  $N$ . This matrix ( $M$ ) projects the  $n \times t$  (number of time points) data matrix ( $Y$ ) on to the nullspace of the homogeneous field. This sensor level data matrix ( $Y$ ) can be modelled as the product of a lead field matrix ( $L$ ) and the underlying neural currents ( $J$ ) in the presence of some random sensor level noise ( $\epsilon$ ) and some spatially homogeneous interfering component ( $H$ ).

$$Y = L J + H + \epsilon \quad (9)$$

If one, multiplies the data ( $Y$ ) by the projector matrix ( $M$ ) the model updates as follows

$$M Y = M L J + M H + M \epsilon \quad (10)$$

As  $M$  projects the data away from the homogeneous field component ( $H$ ) then  $MH = 0$ . Through the following change of variables:  $MY = Y_m$ ,  $ML = L_m$  and  $M\varepsilon = \varepsilon_m$  we can reformulate the model of the sensor level data as follows

$$Y_m = L_m J + \varepsilon_m \quad (11)$$

If we minimize the sum of squared errors ( $\varepsilon_m^t \varepsilon_m$ ) the underlying neural currents can be recovered.

$$J = L_m^{-1} (L_m L_m^{-1}) Y_m \quad (12)$$

It should therefore be clear that if one wishes to perform source reconstruction then one needs to multiply both the lead fields ( $L$ ) and the data  $Y$  by the projector matrix ( $M$ ). Furthermore, this formalism demonstrates that if there is some true signal removed from the data matrix ( $Y$ ) by the projector ( $M$ ) it can be accounted for in subsequent analyses.

### 3. Methods

#### 3.1. Empty room noise demonstration

We postulated that much of the interference magnetometers experience can be modelled as a spatially homogeneous field. All measurements were made in the new UCL magnetically shielded room specifically designed for OP(Optically Pumped)-MEG. The shielded room, constructed by Magnetic Shields Ltd, has internal dimensions of 4377 mm x 3377 mm x 2182 mm and is constructed from two inner layers of 1 mm mu-metal, a 6 mm Copper layer, and then two external layers of 1.5 mm mu-metal.

We provide empirical demonstration by assessing the ability of the basis set,  $N$  to mitigate interference in an empty room noise recording. We placed 31 Gen-2 QuSpin OPMs in a participant specific scanner cast (Boto et al., 2016). We recorded 3 min of empty room noise data with a 16-bit precision ADC (National Instruments) at 6000 Hz sampling rate. We record both the radial and tangential fields from the sensors to double the effective channel count and increase the degrees of freedom.

We performed the analysis as described in Section 2 using  $N$  as the basis set. We also analysed the data using SSP (Uusitalo and Ilmoniemi, 1997) using a separate empty room noise recording for training data. The results of this are not intended to be a definitive comparison but a demonstration of the shielding factors that can be obtained with the proposed correction even in the absence of training data (which is required for SSP). We also demonstrate the effects of a synthetic gradiometer on the empty-room data. For this case we subtracted the output of two parallel sensors separated by distance of ~4 cm. We calculated shielding factors for all methods as a function of frequency.

#### 3.2. Lead field attenuation

Any spatial basis set will share variance (even if only by chance) with the lead fields (the basis set defining the neural subspace). Therefore, a certain percentage of brain signal may be attenuated following this (or any) regression. To directly assess how much variance is shared between the homogeneous field and the lead fields, we regress the homogeneous field ( $N$ ) on to simulated lead fields and calculate the variance explained. The signal attenuation in decibels (dB) can be calculated as  $10 \log_{10}(1 - VE)$ , where  $VE$  is the fraction of shared variance between the lead fields and  $N$ .

For the simulation, the sensor array defining the lead fields was a custom made scanner cast (Boto et al., 2016) with 72 sensor slots. For every sensor position two sensor orientations were simulated (one radial and one tangential to the head). The result was 72 sensors and 144 channels. The brain mesh used to generate these leadfields was the MNI canonical mesh available in SPM12, warped to the anatomy of the individual the custom scanner cast was made for. The separation between vertices is approximately 5 mm on average. The orientation of the source

was defined by the surface normal of the cortical mesh at that location. The forward model was the Nolte single shell model (Nolte, 2003) and sensors were assumed to be point magnetometers.

We also empirically show in phantom recordings (current dipole (10nAm peak to peak) at ~8 cm depth, sinusoidal signal at 10 Hz) of different sensor counts (25 and 35) how the measured field can be attenuated at lower sensor counts by the homogeneous field correction. However as this attenuation is deterministic it can be modelled using the framework provided in Section 2.2.

#### 3.3. Sensor level analysis

Here we show how the proposed approximation can improve the statistical power of sensor level analyses, even during participant motion (~45° rotation) using an auditory evoked response paradigm. One male, aged 26 years, participated in this study and gave informed written consent in line with UCL ethics. The auditory tones had a duration of 70 ms (5 ms rise and fall times) and frequencies of 500–800 Hz in steps of 50 Hz. The inter-stimulus interval was 0.5 s. Stimuli were presented via Psychopy, through MEG-compatible ear tubes with etymotic transducers, and the volume was adjusted to a comfortable level, as specified by the participant. A total of around 1400 individual auditory tones were presented. During the experiment, the participant was instructed to continually, slowly rotate their head by 45° in any direction that was comfortable and to ignore the auditory tones. This was done to deliberately create rotation induced non-stationarities in the recorded data. No motion tracking was performed.

Data were acquired with the same 31 sensors (62 channels) in Section 3.1 at 6000 Hz using a National Instrument 9205 ADC (16 bit system) and subsequently downsampled to 600 Hz. The same homogeneous field correction was applied to the data as in Section 3.1. Data were then band passed filtered between 2 and 40 Hz with a notch at 50 Hz (results in the 1–40 Hz band are presented in supplementary Fig. S1). The data were averaged across trials to observe an evoked response. A one sample Student  $t$ -test was conducted at each time point across trials. Data were corrected for multiple comparisons using Bonferroni correction. For comparison, the same analysis pipeline was repeated but without the use of the homogeneous field correction. The absolute change in field as a function of frequency is presented in supplementary Fig. S2.

We also compared the method directly against DSSP (Sekihara et al., 2016). However, we found that the rank of the leadfields was not greater than the rank of the data. As such correction with DSSP did not result in a change to the data and is therefore not presented. We also investigated whether we could extend the homogeneous field correction to the temporal domain in a manner similar to tSSS (Taulu and Hari, 2009). These results are presented in supplementary Fig. S3.

#### 3.4. Source level analysis

To examine the effect of the homogeneous field correction at the source level, we reconstructed the source space time courses using Minimum Norm (Hämäläinen et al., 1993) as implemented in SPM12 (Friston et al., 2008; Lopez et al., 2014) for both the homogeneous field corrected data and the uncorrected data.

We then (in a similar manner to the sensor level) constructed one-sample  $t$ -tests but this time focusing on the M100 evoked response. The resulting statistical parametric map was smoothed with a 20 mm Gaussian kernel and corrected for multiple comparisons using Bonferroni correction. The squared  $t$ -statistic (across trials) represents the SNR (power) of the evoked response and can be interpreted as an  $F$ -statistic showing at what time points SNR is greater than 0 dB. We calculate these SNR-time series for both the homogeneous field corrected and uncorrected data at the region of highest statistical power (global maximum). We also calculate how this SNR varies with distance from the global maximum to measure the Full Width at Half Maximum (FWHM) of the SNR.

### 3.5. Software

All analysis was carried out using the SPM12 (<https://www.fil.ion.ucl.ac.uk/spm/>) software package and custom Matlab scripts. All software is freely available via GitHub (<https://github.com/tierneytim/>

OPM). The relevant function is called `spm_opm_mfc.m` and example code and data is available in the repository. This code not only performs the correction to the sensor level data but also sets a flag such that if lead fields are generated they will automatically be corrected with the appropriate projection matrix.

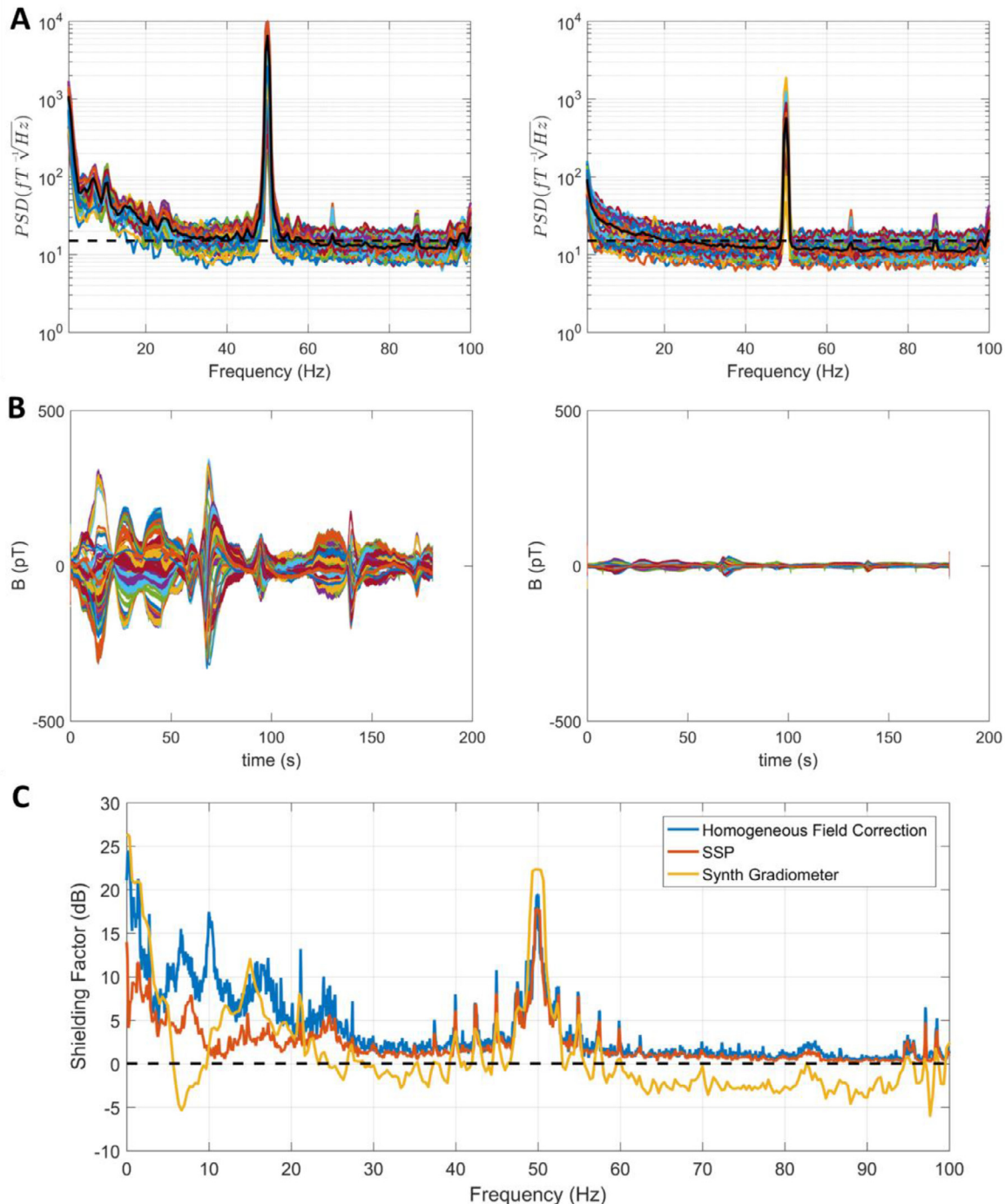


**Fig. 1.** Homogeneous field correction for empty room noise data. In (A) the power spectral density (rms) is displayed for both uncorrected data (left) and corrected data (right). The average power spectral density is highlighted in black. The dotted black line is at  $15 \text{ pT}/\sqrt{\text{Hz}}$ . Large sources of interference (drift, 50 Hz) experienced a 10-fold reduction in magnitude while nearly 5-fold reduction in interference was observed between 5 and 20 Hz. In (B) representative time segments are shown. The uncorrected data in the left panel show that the environmental noise within the room could change quickly by a few hundred picotesla. Whereas in the corrected time series (right) these changes were reduced to the order of tens of picotesla. In (C) the average shielding factor across the 62 channels in decibels (dB) is plotted as a function of frequency for both the homogeneous field correction and the Signal Space Projection method. We also plot the shielding factor of two aligned magnetometers at a distance of  $\sim 4 \text{ cm}$  (synthetic gradiometers). There is a positive effect across the entire bandwidth analysed (0–100 Hz) for both the homogeneous field method and the SSP method. At higher frequencies, the synthetic gradiometer introduces more noise than it corrects as the intrinsic white noise from the two sensors adds in quadrature.

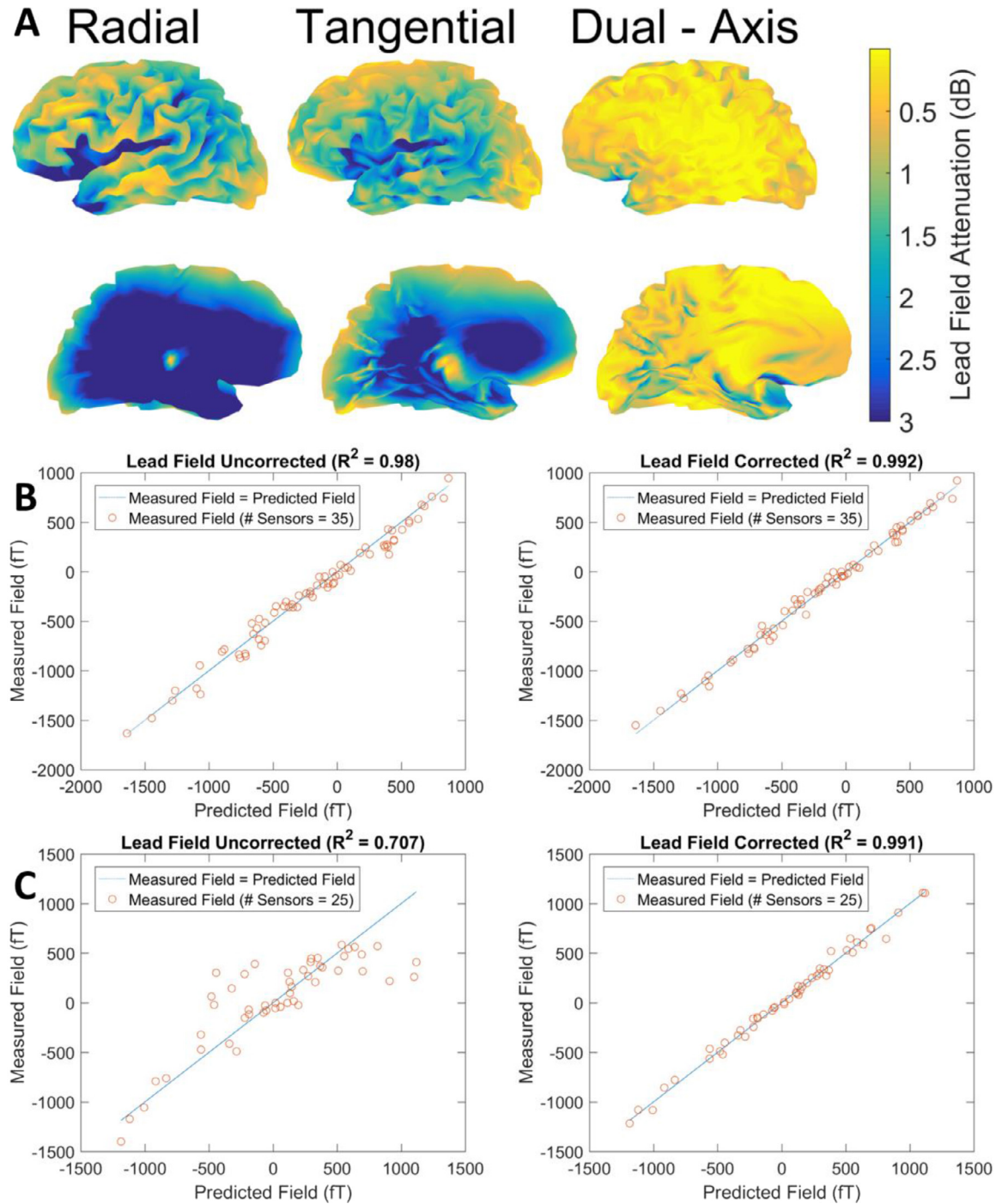


**Fig. 2.** Theoretical (A) and empirical (B & C) demonstration of Lead field attenuation for homogeneous field correction. In (A) For the 72 sensor system the lead-field attenuation (expressed as signal loss in dB, larger values indicating greater signal loss) is shown for sensors measuring radially, tangentially and in dual axis mode. It is clear that the deeper sources share more variance with the homogeneous field basis set but this effect is greatly diminished when data are collected in dual axis mode. In (B) and (C): predicted vs. measured magnetic field of a dipole phantom (10 nAm peak to peak, 10 Hz sinusoidal activation at a surface-to-source depth of  $\sim 8$  cm), as sampled by OPM arrays with different numbers of sensors. Each point represents the sample of a single sensor orientation (each sensor measures a radial and tangential component resulting in 50 measurements for 25 sensors and 70 measurements for 35 sensors). The blue line is a guide to the eye for the ideal situation when the measured and predicted fields are exactly equal. Left/right-hand columns: measured data uncorrected/corrected for the lead-field attenuation induced by homogeneous field removal. In a system with 35 sensors, the lead fields are relatively unaffected by the homogeneous field removal (B, left-hand panel), but correcting for the lead field attenuation (see Section 2.2) improves the match between measured and predicted sampled field values (B, right-hand panel). For the lower sensor count (25 sensors), the measured field is noticeably attenuated by the homogeneous field removal (C, left-hand panel), but accounting for the lead-field attenuation (see Section 2.2) allows for a significant reduction of this unwanted effect (C, right-hand panel) (For interpretation of the references to color in this figure legend, the reader is referred to the web version of this article.).

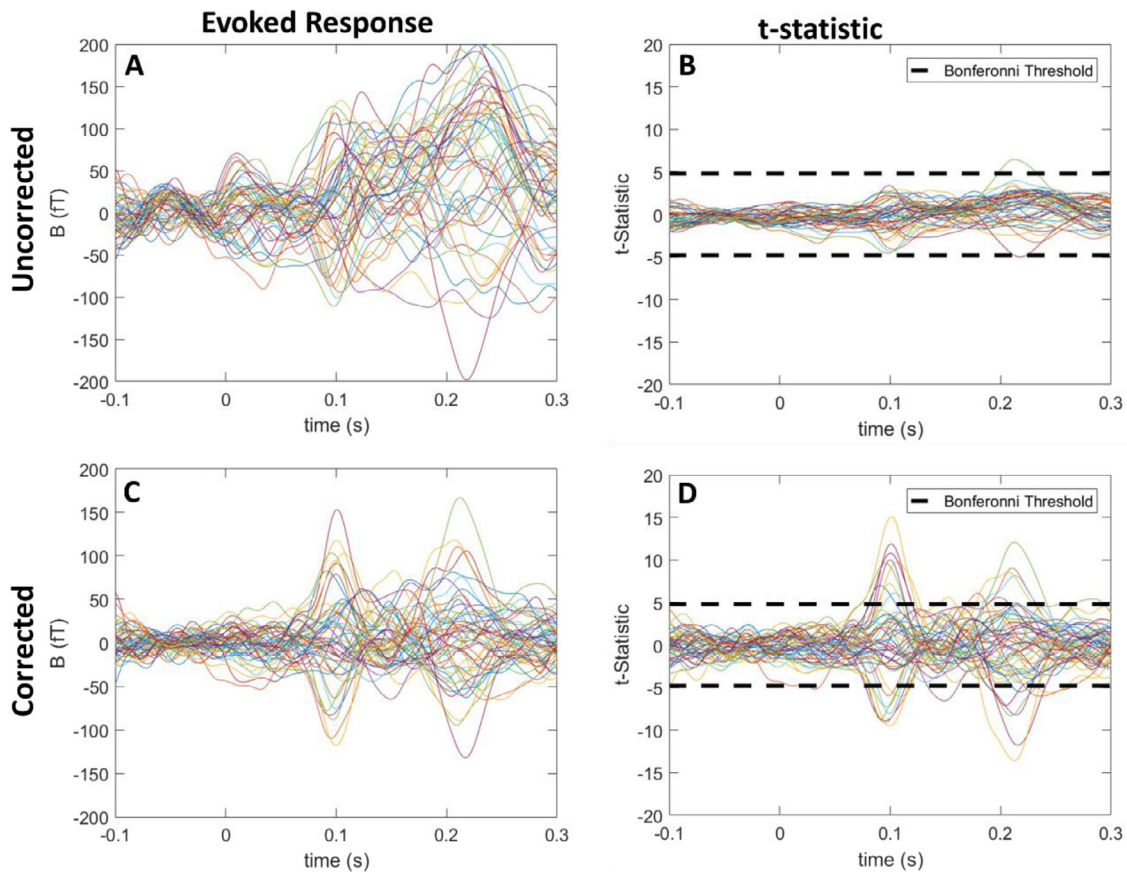


**Fig. 3.** Interference correction in the presence of motion. In (A) and (B) the evoked response and associated t-statistics are shown for the auditory evoked response when no correction is applied. The 100 ms and 200 ms response are difficult to discern from the data and the statistical efficiency is poor due to the high level of variation. However, in (C) and (D) when the homogeneous field correction is applied both the 100 ms and 200 ms response are clearly visible in both the evoked response and the t-statistic.

## 4. Results

### 4.1. Empty room demonstration

In the empty room recordings (see Fig. 1) the drift ( $<1$  Hz) and 50 Hz components are reduced by a factor of 10 (20 dB), whereas the vibration components within the 3 and 20 Hz band are reduced by up to a factor of 5 (15 dB). It is important to note that this improvement was achieved by using only the 3 regressors of the basis  $N$ . The noise floor reached 10fT at higher frequencies. These reductions provide an empirical verification that the homogeneous field approximations does indeed explain a majority of variance in the magnetic interference encountered in our magnetically shielded room. Encouragingly, these shielding factors are obtained without the need for training data. If training data are available SSP can be performed as in Fig. 1c. Alternatively one could create a synthetic gradiometer by subtracting the output of two magnetometers. While this approach can show strong interference suppression it increases the white noise component by  $\sqrt{2}$ . This effect is visible in Fig. 1c as at high frequencies the noise increases by 3 dB.

### 4.2. Lead field attenuation

We next examined whether the proposed homogeneous field correction attenuated useful signal as well as interference. As is apparent in Fig. 2A, the signal attenuation was, on average, less than 0.5 dB for an array consisting of both radial and tangential OPMs. It reaches a maximum of  $\sim 1.5$  dB for the combined array and, as such, the reduction in noise observed in Fig. 1 outweighs any signal loss. What is perhaps most interesting here is that the signal loss is much lower for a dual-axis recording

as opposed to recordings from either axis individually. There is also a clear pattern of increased signal loss at depth with single axis recordings, although, this effect is mitigated by dual-axis recordings. While this attenuation cannot be undone, it can be accounted for in source analyses for any sensor count. We show in Fig. 2B and 2C that the effects are deterministic in a phantom recording (current dipole at  $\sim 8$  cm depth, sinusoidal signal at 10 Hz) of different sensor counts (25 and 35) and can be modelled using the framework provided in Section 2.2. At lower sensor counts (25), the effects were much worse than at higher sensor counts (35) but easily accounted for in both cases.

### 4.3. Sensor level analysis

As shown in Fig. 3, we assessed OPM measured auditory evoked responses during movement ( $\sim 45^\circ$  rotation). The sensor level evoked response (in Fig. 3A and 3B) was obscured across many sensors due to trial to trial variation. However, when the homogeneous field correction was applied, the evoked response became much clearer (Fig. 3C) and the reduction in trial to trial variation was reflected in the increased magnitude of the t-statistics (Fig. 3D).

### 4.4. Source level demonstration

The source-level SPMs were both broadly similar for corrected and uncorrected data but the homogeneous field corrected data had more supra-threshold vertices and higher statistical power (Fig. 4A and 4B). When we looked directly at how the SNR changed over space (Fig. 4C) we observed that the FWHM of the SNR was comparable between both methods, but the SNR was higher for the homogeneous field corrected

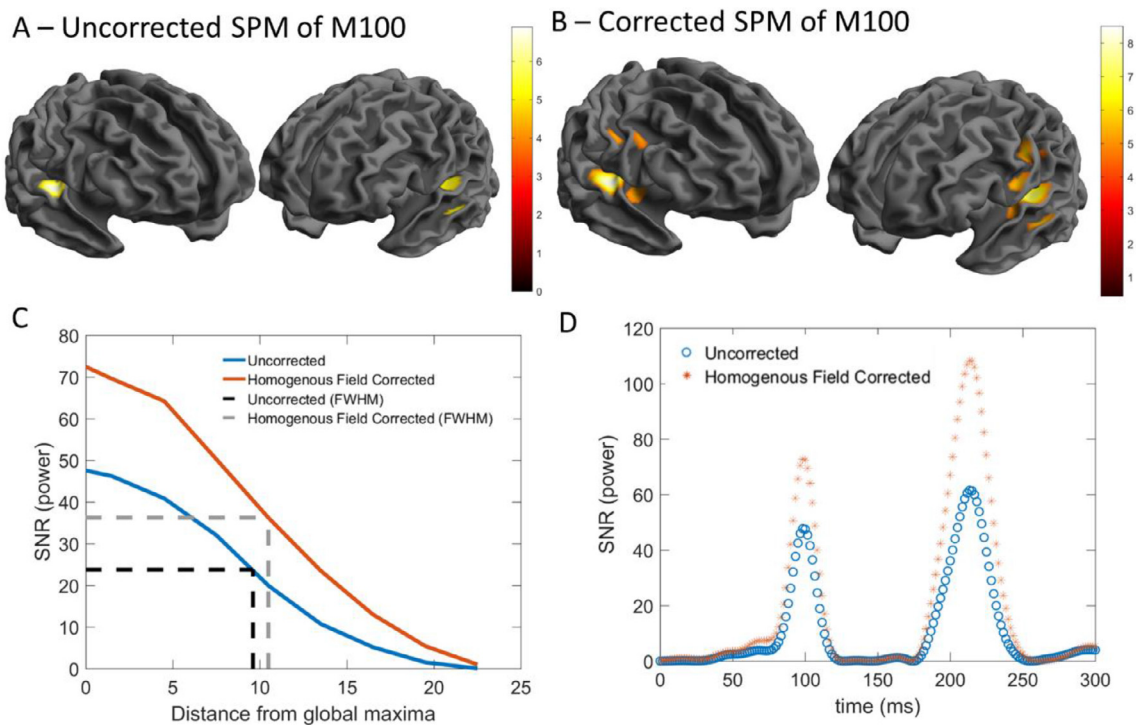


**Fig. 4.** Source level results. In (A) and (B), statistical parametric maps ( $t$ -statistic) are shown for the 100 ms response to auditory stimuli for both the uncorrected and homogeneous field corrected data respectively. Both situations resulted in bilateral maxima observed in auditory cortex. In (C) the SNR as a function of space is shown. Both methods had comparable FWHMs but the homogeneous field corrected data had better SNR. In (D) the SNR (power) is shown over time for both methods. The homogeneous field method reconstructed more power in the auditory cortex with higher SNR for both the 100 ms component as well as the 200 ms component.

data. We also directly calculated the SNR across trials (power) at every time point for both methods. This can be interpreted as an F-statistic and clearly showed that the homogeneous field corrected data had better source level SNR than the uncorrected data (Fig. 4D) at the time points of high signal (100 ms and 200 ms).

## 5. Discussion

In this study we demonstrated that a homogeneous field correction provides a simple but powerful approach for the reduction of interference observed by OPMs.

The correction we propose adds to the existing model-based software approaches for the separation of signal from interference. The attraction of using such a low order model lies in both the simplicity of implementation and the low likelihood of removing neural signal. As sensor numbers in OPM arrays are currently much lower than cryogenic MEG systems, the likelihood that any spatial basis set will explain some neural signal by chance is increased. As such, default settings for current spatial denoising algorithms may not be appropriate, and will need to be adjusted for OPM experiments. However, it is worth noting that for OPM arrays that provide spatial oversampling (i.e., as SQUID-based MEG systems typically do), the issues related to the use of higher order models will be less of a concern. Theoretically, this method could be extended to incorporate a temporally extended version similar to tSSS (Taulu and Hari, 2009). tSSS requires the definition of a noise-subspace and, as already noted, for some arrays there will be a non-negligible correlation between a given basis set and a lead field. We show in supplementary material that the addition of this temporal extension does not markedly improve performance for this particular experiment (Fig. S3). However, this is an interesting area for future research.

An alternative and powerful model based approach lies in the use of DSSP (Sekihara et al., 2016) which uses the eigenmodes of the lead

fields as a spatial basis set to explain the data (effectively modelling the neural subspace at the sensor level). For the array used in this study we found that as the rank of the lead fields was the same as the rank of the data the external subspace was poorly defined and DSSP was not appropriate for removing interference from the data (not shown). We expect this method to be much more powerful on spatially oversampled data, such as that offered by the new, 432 channel, Kernel Flux system (Pratt et al., 2021).

More data driven approaches lie in the use of adaptive source reconstruction techniques such as beamformers (Belardinelli et al., 2012; Van Veen and Buckley, 1988). In principle, for stationary participants, the homogeneous field correction will be of little benefit for beamformer studies (unless the interference covariance changes over time). However, for moving participants, the beamformer may be less effective at removing correlated interference because the estimate of the covariance matrix will be inefficient and biased due to movement induced non-stationarities (although see (Woolrich et al. 2013) for a non-stationary implementation). Ultimately, the homogeneous field correction suggested here offers a compromise between model complexity, variance shared with the leadfields, ease of implementation and non-stationary interference reduction.

While the proposed correction can help improve the quality of data in OPM experiments using a very low order model, it has some limitations. Most notably, the basis set will have some small correlation with the leadfields. This correlation gets smaller with increased number of sensors and simultaneous multi-axis measurements but it nevertheless still exists. The effect of this will depend on the array geometry, sensor design and sensor number. The simulation results here clearly point to the utility of multi-axis measurements to help mitigate this problem. With regards to sensor numbers one can reproduce the analysis of Fig. 2 for any channel count/positioning or subject specific anatomy and weigh up the expected signal loss with the observed interference reduction.

We should note that our empirical validation of the lead-field attenuation was not exhaustive but used a single magnetic dipole displaced 8 cm from the sensor array (i.e. close to the centre of the head in a recording scenario). We did this in order to characterize the worst-case scenario where lead-field attenuation is maximal. Encouragingly, the findings accord well with our theoretical predictions that the lead field attenuation is deterministic.

An issue associated with array geometry is the requirement for accurate knowledge of the sensors' sensitive axis. This may be slightly different from the physical orientation of the sensor due to the presence of cross-talk (Tierney et al., 2019) or imperfect on board coil design. This issue may be more pronounced for densely packed arrays of OPMs. However, such issues can be reduced by operating the sensors with coils specifically designed to reduce cross-talk (Nardelli et al., 2019) or by the use of data driven approaches which can learn sensor sensitive axes from the data (Duque-Muñoz et al., 2019).

Necessarily, OPMs operate with the aid of on board magnetic coils to maintain zero field at the sensor (Osborne et al., 2018; Tierney et al., 2019). If the magnetic field from these on board coils is not updated as the field at the sensor changes, there will be a component of the motion artefact that is a function of this initial sensor specific magnetic field (e.g. when someone rotates their head the magnetic field designed to keep zero field in one orientation will be incorrectly applied to a different orientation). We do not investigate this effect here but note that it could be mitigated by operating sensors in a closed loop mode (Nardelli et al., 2020), learning this field profile directly from the data itself or by utilizing active shielding so as to keep these values to a minimum (Holmes et al., 2018, 2019; Iivanainen et al., 2019a). A further benefit using a closed-loop sensor or active shielding would be the minimization of gain changes due to field drifts or excessive motion (Iivanainen et al., 2019b; Nardelli et al., 2020). Eliminating these gain changes is not just important for accurate source reconstruction but also for maximizing the shielding factors provided by software correction methods (Taulu et al., 2005).

While these issues will be the subject of future work, the data presented here show that a simple homogeneous field correction can mitigate much of the interference observed in OPM recordings and improve statistical power both temporally and spatially at sensor and source level. This approximation benefits from multi-axis measurement and, in this case, has minimal negative impact on the neural subspace. These features, coupled with its ease of implementation and lack of reliance on knowledge of the underlying neuroanatomy, render this an appealing and powerful preprocessing step for arrays of OPMs.

#### Data and code availability statements

Data is to be made available via a request to the Authors. All data was processed using SPM 12 (<https://www.fil.ion.ucl.ac.uk/spm/software/spm12/>) and additional functions are made publicly available on the first author's GitHub page (<https://github.com/tierneytim/OPM>).

#### Credit authorship contribution statement

**Tim M. Tierney:** Conceptualization, Methodology, Software, Writing – review & editing, Writing – original draft. **Nicholas Alexander:** Data curation, Writing – review & editing, Writing – original draft, Methodology. **Stephanie Mellor:** Conceptualization, Writing – review & editing, Writing – original draft. **Niall Holmes:** Conceptualization, Writing – review & editing, Writing – original draft. **Robert Seymour:** Data curation, Writing – review & editing, Writing – original draft, Methodology. **George C. O'Neill:** Software, Writing – review & editing, Writing – original draft. **Eleanor A. Maguire:** Writing – review & editing, Writing – original draft, Methodology. **Gareth R. Barnes:** Writing – review & editing, Writing – original draft, Methodology, Conceptualization.

#### Acknowledgments

This work was supported by a Wellcome collaborative award to GRB, Matthew Brookes and Richard Bowtell (203257/Z/16/Z, 203257/B/16/Z). SM was funded through the EPSRC-funded UCL Centre for Doctoral Training in Medical Imaging (EP/L016478/1) and GO through EPSRC (EP/T001046/1) funding from the Quantum Technology hub in sensing and timing (sub-award QTPRF02). The Wellcome Centre for Human Neuroimaging is supported by core funding from the Wellcome Trust (203147/Z/16/Z). EAM is funded through a Wellcome Principal Research fellowship (210567/Z/18/Z). We also would like to thank the Matthew Brookes, Richard Bowtell, Vishal Shah and David Woolger and their respective teams at University of Nottingham, QuSpin and Magnetic Shields Ltd for their support throughout the development of our OPM system. We would also like to acknowledge the support of Mark Lim of Chalk Studios in designing the 3D printed scanner-casts used in this study.

#### Supplementary materials

Supplementary material associated with this article can be found, in the online version, at [doi:10.1016/j.neuroimage.2021.118484](https://doi.org/10.1016/j.neuroimage.2021.118484).

#### Appendix A. Derivation of correction method using Signal Space Separation

In the theory section we used a simple argument to derive a model of homogeneous interference correction based on the relationships between the measured signal and the sensor orientations. An equivalent derivation can be reached by examining the SSS method (Taulu and Kajola, 2005). SSS represents the MEG signal ( $B$ ) as a linear combination of the gradients of spherical harmonics ( $Y_{lm}(\theta, \varphi)$ ) with coefficients  $\alpha_{lm}$  and  $\beta_{lm}$ . The full formulation for the magnetic field in spherical coordinates ( $r, \theta, \varphi$ ) is

$$B(r, \theta, \varphi) = -\mu_0 \sum_{l=0}^{\infty} \sum_{m=-l}^l \alpha_{lm} \nabla \left[ \frac{Y_{lm}(\theta, \varphi)}{r^{l+1}} \right] - \mu_0 \sum_{l=0}^{\infty} \sum_{m=-l}^l \beta_{lm} \nabla [r^l Y_{lm}(\theta, \varphi)] \quad (A1)$$

The first term represents the neural space while the second term represents the interference space. If we truncate the interference space to  $l = 1$  the interference term reduces to a vector of some constant values ( $a, b, c$ ) that do not change over space. For now, we represent the interior signal space by vector components ( $B_{xin}, B_{yin}, B_{zin}$ ) that can be defined at any point in space. We can therefore describe the magnetic field vector components ( $B_x, B_y, B_z$ ) at any location as follows:

$$B(r, \theta, \varphi) = \begin{pmatrix} B_x \\ B_y \\ B_z \end{pmatrix} = \begin{pmatrix} B_{xin}(r, \theta, \varphi) \\ B_{yin}(r, \theta, \varphi) \\ B_{zin}(r, \theta, \varphi) \end{pmatrix} + \begin{pmatrix} a \\ b \\ c \end{pmatrix} \quad (A2)$$

If we want the field measured by a sensor, we simply need take the inner product of the magnetic field vector with the sensor's sensitive axis. Measurements made at multiple points in space can be described in the following matrix form

$$B_{measured} = \begin{pmatrix} o_x^1 B_{xin}(r_1, \theta_1, \varphi_1) + o_y^1 B_{yin}(r_1, \theta_1, \varphi_1) + o_z^1 B_{zin}(r_1, \theta_1, \varphi_1) \\ \vdots \\ o_x^n B_{xin}(r_n, \theta_n, \varphi_n) + o_y^n B_{yin}(r_n, \theta_n, \varphi_n) + o_z^n B_{zin}(r_n, \theta_n, \varphi_n) \end{pmatrix} + \begin{pmatrix} o_x^1 a + o_y^1 b + o_z^1 c \\ \vdots \\ o_x^n a + o_y^n b + o_z^n c \end{pmatrix} \quad (A3)$$

Here  $o_x^i, o_y^i, o_z^i$  represent the orientation of the sensitive axis the  $i^{th}$  sensor. The position dependant terms, which represent the signal space, can now be modelled as the product of the lead fields ( $L$ ) and underlying neural currents ( $J$ ) while the position independent terms can be

described by the matrix product of the sensor normal matrix ( $N$ ) and the homogeneous field coefficients ( $a, b, c$ ).

$$B_{measured} = LJ + N \begin{pmatrix} a \\ b \\ c \end{pmatrix} \quad (A4)$$

If the measured field is multiplied by the projector matrix ( $M = I - NN^+$ ) the model updates as follows

$$MB_{measured} = MLJ + (N - NN^+N) \begin{pmatrix} a \\ b \\ c \end{pmatrix} \quad (A5)$$

As  $NN^+N = N$  then the second term tends to zero and the underlying neural currents can be recovered as follows

$$J = L_m^{-1} (L_m L_m^{-1}) Y_m \quad (A6)$$

Where  $L_m = ML$  and  $Y_m = MB_{measured}$ . We now have an identical result for  $J$  as presented in the theory section of this paper. Essentially the proposed method projects the signal space onto the lead fields and the interference space on to the lowest order ( $l = 1$ ), position independent terms of the SSS basis.

## References

- Allred, J.C., Lyman, R.N., Kornack, T.W., Romalis, M.V., 2002. High-sensitivity atomic magnetometer unaffected by spin-exchange relaxation. *Phys. Rev. Lett.* 89 (13), 130801. doi:10.1103/PhysRevLett.89.130801.
- Barry, D.N., Tierney, T.M., Holmes, N., Boto, E., Roberts, G., Leggett, J., Bowtell, R., Brookes, M.J., Barnes, G.R., Maguire, E.A., 2019. Imaging the human hippocampus with optically-pumped magnetoencephalography. *NeuroImage* 203, 116192. doi:10.1016/j.neuroimage.2019.116192.
- Belardinelli, P., Ortiz, E., Barnes, G., Noppeney, U., Preissl, H., 2012. Source reconstruction accuracy of MEG and EEG Bayesian inversion approaches. *PLoS ONE* 7 (12). doi:10.1371/journal.pone.0051985.
- Boto, E., Holmes, N., Leggett, J., Roberts, G., Shah, V., Meyer, S.S.S., Muñoz, L.D.L.D., Mullinger, K.J.K.J., Tierney, T.M.T.M., Bestmann, S., Barnes, G.R., Bowtell, R., Brookes, M.J.M.J., 2018. Moving magnetoencephalography towards real-world applications with a wearable system. *Nature* 555 (7698), 657–661. doi:10.1038/nature26147.
- Boto, E., Meyer, S.S., Shah, V., Alem, O., Knappe, S., Kruger, P., Fromhold, M., Lim, M., Morris, P.G., Bowtell, R., Barnes, G.R., Brookes, M.J., 2016. A new generation of magnetoencephalography: room temperature measurements using optically-pumped magnetometers. *NeuroImage* 1. doi:10.1016/j.neuroimage.2017.01.034.
- Boto, E., Seedat, Z.A., Holmes, N., Leggett, J., Hill, R.M., Roberts, G., Shah, V., Fromhold, T.M., Mullinger, K.J., Tierney, T.M., Barnes, G.R., Bowtell, R., Brookes, M.J., 2019. Wearable neuroimaging: combining and contrasting magnetoencephalography and electroencephalography. *NeuroImage* 201 (June), 116099. doi:10.1016/j.neuroimage.2019.116099.
- Colombo, A.P., Carter, T.R., Borna, A., Jau, Y.Y., Johnson, C.N., Dagele, A.L., Schwindt, P.D.D., 2016. Four-channel optically pumped atomic magnetometer for magnetoencephalography. *Opt. Express* 24 (14), 15403. doi:10.1364/OE.24.015403.
- de Cheveigné, A., 2020. ZapLine: a simple and effective method to remove power line artifacts. *NeuroImage* 207. doi:10.1016/j.neuroimage.2019.116356.
- Duque-Muñoz, L., Tierney, T.M., Meyer, S.S., Boto, E., Roberts, G., Leggett, J., Bowtell, R., Brookes, M.J., López, J.D., Barnes, G.R., 2019. Data-driven model optimization for optically pumped magnetometer sensor arrays. *Hum. Brain Mapp.* (June) 1–13. doi:10.1002/hbm.24707.
- Fife, A.A., Vrba, J., Robinson, S.E., Anderson, G., Betts, K., Burbank, M.B., 1999. Synthetic gradiometer systems for MEG. *IEEE Trans. Appl. Supercond.* 9 (2 PART 3), 4063–4068. doi:10.1109/77.783919.
- Friston, K., Harrison, L., Daunizeau, J., Kiebel, S., Phillips, C., Trujillo-Barreto, N., Henson, R., Flandin, G., Mattout, J., 2008. Multiple sparse priors for the M/EEG inverse problem. *NeuroImage* 39 (3), 1104–1120. doi:10.1016/j.neuroimage.2007.09.048.
- Golub, G.H., Van Loan, C.F., 1996. *Matrix Computations*, 3rd ed. The Johns Hopkins University Press Baltimore.
- Hämäläinen, M., Hari, R., Ilmoniemi, R.J., Knuutila, J., Lounasmaa, O.V., 1993. Magnetoencephalography theory, instrumentation, and applications to noninvasive studies of the working human brain. *Rev. Mod. Phys.* 65 (2), 413–497. doi:10.1103/RevModPhys.65.413.
- Hill, R.M., Boto, E., Rea, M., Holmes, N., Leggett, J., Coles, L.A., Papastavrou, M., Evertson, S., Hunt, B.A.E., Sims, D., Osborne, J., Shah, V., Bowtell, R., Brookes, M.J., 2020. Multi-channel whole-head OPM-MEG: helmet design and a comparison with a conventional system. *NeuroImage*, 116995. doi:10.1016/j.neuroimage.2020.116995.
- Holmes, N., Leggett, J., Boto, E., Roberts, G., Hill, R.M., Tierney, T.M., Shah, V., Barnes, G.R., Brookes, M.J., Bowtell, R., 2018. A bi-planar coil system for nulling background magnetic fields in scalp mounted magnetoencephalography. *NeuroImage* 181 (July), 760–774. doi:10.1016/j.neuroimage.2018.07.028.
- Holmes, N., Tierney, T.M., Leggett, J., Boto, E., Stephanie, M., Roberts, G., Hill, R.M., Shah, V., Barnes, G.R., Brookes, M.J., Bowtell, R., 2019. Balanced, bi-planar magnetic field and field gradient coils for field compensation in wearable magnetoencephalography. *Sci. Rep.* (January) 1–15. doi:10.1038/s41598-019-50697-w.
- Iivanainen, J., Mäkinen, A. J., Zetter, R., Stenroos, M., Ilmoniemi, R. J., & Parkkonen, L. (2020). Spatial sampling of MEG and EEG revisited: From spatial-frequency spectra to model-informed sampling. Retrieved from <http://arxiv.org/abs/2006.02919>
- Iivanainen, J., Zetter, R., Grön, M., Hakkarainen, K., Parkkonen, L., 2019a. On-scalp MEG system utilizing an actively shielded array of optically-pumped magnetometers. *NeuroImage* 194 (March), 244–258. doi:10.1016/j.neuroimage.2019.03.022.
- Iivanainen, J., Zetter, R., Parkkonen, L., 2019b. Potential of on-scalp MEG: robust detection of human visual gamma-band responses. *Hum. Brain Mapp.* (April) 1–12. doi:10.1002/hbm.24795.
- Kominis, I.K., Kornack, T.W., Allred, J.C., Romalis, M.V., 2003. A subfemtotesla multichannel atomic magnetometer. *Nature* 422 (6932), 596–599. doi:10.1038/nature01484.
- Limes, M.E., Foley, E.L., Kornack, T.W., Caliga, S., McBride, S., Braun, A., Lee, W., Lucivero, V.G., & Romalis, M.V. (2020). Total-field atomic gradiometer for unshielded portable magnetoencephalography. *Arxiv*, 1–8. Retrieved from <http://arxiv.org/abs/2001.03534>
- Lin, C.-H., Tierney, T.M., Holmes, N., Boto, E., Leggett, J., Bestmann, S., Bowtell, R., Brookes, M.J., Barnes, G.R., Miall, R.C., 2019. Using optically-pumped magnetometers to measure magnetoencephalographic signals in the human cerebellum. *J. Physiol.* (Lond.) 0, 1–16. doi:10.1113/jp277899.
- Lopez, J.D., Litvak, V., Espinosa, J.J., Friston, K., Barnes, G.R., 2014. Algorithmic procedures for Bayesian MEG/EEG source reconstruction in SPM. *NeuroImage* 84, 476–487. doi:10.1016/j.neuroimage.2013.09.002.
- Nardelli, N.V., Krzyzewski, S.P., Knappe, S.A., 2019. Reducing crosstalk in optically-pumped magnetometer arrays. *Phys. Med. Biol.* (21) 64. doi:10.1088/1361-6560/ab4c06.
- Nardelli, N.V., Perry, A.R., Krzyzewski, S.P., Knappe, S.A., 2020. A conformal array of microfabricated optically-pumped first-order gradiometers for magnetoencephalography. *EPJ Quantum Technol.* 7 (1). doi:10.1140/epjqt/s40507-020-00086-4.
- Neonen, J., Taulu, S., Kajola, M., Ahonen, A., 2007. Total information extracted from MEG measurements. *Int. Congr. Ser.* 1300, 245–248. doi:10.1016/j.ics.2007.01.058.
- Nolte, G., 2003. The magnetic lead field theorem in the quasi-static approximation and its use for magnetoencephalography forward calculation in realistic volume conductors. *Phys. Med. Biol.* 48 (22), 3637–3652. doi:10.1088/0031-9155/48/22/002.
- Okada, Y., Hämäläinen, M., Pratt, K., Mascarenas, A., Miller, P., Han, M., Robles, J., Cavallini, A., Power, B., Sieng, K., Sun, L., Lew, S., Doshi, C., Ahtam, B., Dinh, C., Esch, L., Grant, E., Paulson, D., 2016. BabyMEG: a whole-head pediatric magnetoencephalography system for human brain development research. *Rev. Sci. Instrum.* 87 (9). doi:10.1063/1.4962020.
- Osborne, J., Orton, J., Alem, O., Shah, V., 2018. Fully integrated, standalone zero field optically pumped magnetometer for biomagnetism. In: Shahriar, S.M., Scheuer, J. (Eds.), *Proceedings of the Steep Dispersion Engineering and Opto-Atomic Precision Metrology XI*, p. 51. doi:10.1117/12.2299197.
- Pratt, Ethan, Ledbetter, Micah, Jiménez-Martínez, Ricardo, Shapiro, Benjamin, Solon, Amelia, Geoffreylwata, Z., Steve Garber, Jeff Gormley, Decker, Dakota, Delgadoillo, David, ArgyriosDellis, T., Jake Phillips, Guhan Sundar, Jerry Leung, Jim Coyne, Mike McKinley, Gilbert Lopez, Scott Homan, Lucas Marsh, Mary Zhang, Vincent Maurice, Benjamin Siesper, Teresa, Giovannoli, Brandon Leverett, Lerner, Gabriel, Scott Seidman, Vicente DeLuna, Wright-Freeman, Kayla, Kates-Harbeck, Julian, Teague Lasser, Hooman Mohseni, Sharp, T.J., Anthony Zorzos, AntonioLara, H., Ali Kouhadi, Alejandro Ojeda, Pronoy Chopra, Zachary Bednarke, Henninger, Michael, JamuAlford, K., 2021. Kernel Flux: a whole-head 432-magnetometer optically-pumped magnetoencephalography (OP-MEG) system for brain activity imaging during natural human experiences. *Proc. SPIE* 11700, Optical and Quantum Sensing and Precision Metrology 1170032. <https://doi.org/10.1117/12.2581794>.
- Sekihara, K., Kawabata, Y., Ushio, S., Sumiya, S., Kawabata, S., Adachi, Y., Nagaran, S.S., 2016. Dual signal subspace projection (DSSP): a novel algorithm for removing large interference in biomagnetic measurements. *J. Neural. Eng.* 13 (3). doi:10.1088/1741-2560/13/3/036007.
- Sheng, D., Perry, A.R., Krzyzewski, S.P., Geller, S., Kitching, J., Knappe, S., 2017. A microfabricated optically-pumped magnetic gradiometer. *Appl. Phys. Lett.* 110 (3), 3–7. doi:10.1063/1.4974349.
- Taulu, S., Hari, R., 2009. Removal of magnetoencephalographic artifacts with temporal signal-space separation: demonstration with single-trial auditory-evoked responses. *Hum. Brain Mapp.* 30 (5), 1524–1534. doi:10.1002/hbm.20627.
- Taulu, S., Kajola, M., 2005. Presentation of electromagnetic multichannel data: the signal space separation method. *J. Appl. Phys.* (12) 97. doi:10.1063/1.1935742.
- Taulu, S., Simola, J., Kajola, M., 2005. Applications of the signal space separation method. *IEEE Trans. Signal Process.* 53 (9), 3359–3372. doi:10.1109/TSP.2005.853302.
- Tierney, T.M., Holmes, N., Mellor, S., López, J.D., Roberts, G., Hill, R.M., Boto, E., Leggett, J., Shah, V., Brookes, M.J., Bowtell, R., Barnes, G.R., 2019. Optically pumped magnetometers: from quantum origins to multi-channel magnetoencephalography. *NeuroImage* 199 (December 2018), 598–608. doi:10.1016/j.neuroimage.2019.05.063.
- Tierney, T.M., Holmes, N., Meyer, S.S., Boto, E., Roberts, G., Leggett, J., Buck, S., Duque-Muñoz, L., Litvak, V., Bestmann, S., Baldeweg, T., Bowtell, R., Brookes, M.J., Barnes, G.R., 2018. Cognitive neuroscience using wearable magnetometer arrays: non-invasive assessment of language function. *NeuroImage* 181 (July), 513–520. doi:10.1016/j.neuroimage.2018.07.035.
- Tierney, T.M., Levy, A., Barry, D., Meyer, S., Shigihara, Y., Everatt, M., Mellor, S., Lopez, J.D., Bestmann, S., Holmes, N., Roberts, G., Hill, R., Boto, E., Leggett, J., Shah, V., Brookes, M., Bowtell, R., Barnes, G., 2020a. Mouth magnetoencephalography: a unique perspective on the human hippocampus. *NeuroImage* 225 (October 2020), 117443. doi:10.1101/2020.03.19.998641.

- Tierney, T.M., Mellor, S., O'Neill, G.C., Holmes, N., Boto, E., Roberts, G., Hill, R.M., Leggett, J., Bowtell, R., Brookes, M.J., Barnes, G.R., 2020b. Pragmatic spatial sampling for wearable MEG arrays. *Scientific Reports* 10 (1), 21609. doi:[10.1038/s41598-020-77589-8](https://doi.org/10.1038/s41598-020-77589-8).
- Uusitalo, M.A., Ilmoniemi, R.J., 1997. Signal-space projection method for separating MEG or EEG into components. *Med. Biol. Eng. Comput.* 35 (2), 135–140. doi:[10.1007/BF02534144](https://doi.org/10.1007/BF02534144).
- Van Veen, B.D., Buckley, K.M., 1988. Beamforming: a versatile approach to spatial filtering. *IEEE ASSP Mag.* 5 (2), 4–24. doi:[10.1109/53.665](https://doi.org/10.1109/53.665).
- Vivekananda, U., Mellor, S., Tierney, T.M., Holmes, N., Boto, E., Leggett, J., Roberts, G., Hill, R., Litvak, V., Brookes, M.J., Bowtell, R., Barnes, G.R., Walker, M., 2020. Optically pumped magnetoencephalography in Epilepsy. *Ann. Clin. Transl. Neurol.* doi:[10.1002/acn3.50995](https://doi.org/10.1002/acn3.50995), In press.
- Vrba, J., Robinson, S.E., 2002. SQUID sensor array configurations for magnetoencephalography applications. *Supercond. Sci. Technol.* 15, 51–89 TOPICAL.
- Woolrich, M.W., Baker, A., Luckhoo, H., Mohseni, H., Barnes, G., Brookes, M., Rezek, L., 2013. Dynamic state allocation for MEG source reconstruction. *NeuroImage* 77, 77–92. doi:[10.1016/j.neuroimage.2013.03.036](https://doi.org/10.1016/j.neuroimage.2013.03.036).